

Distributed model building and recursive integration for big spatial data modeling

Emily C. Hector*

Department of Statistics, North Carolina State University

Brian J. Reich

Department of Statistics, North Carolina State University

Ani Eloyan

Department of Biostatistics, Brown University

Abstract

Motivated by the need for computationally tractable spatial methods in neuroimaging studies, we develop a distributed and integrated framework for estimation and inference of Gaussian process model parameters with ultra-high-dimensional likelihoods. We propose a shift in viewpoint from whole to local data perspectives that is rooted in distributed model building and integrated estimation and inference. The framework's backbone is a computationally and statistically efficient integration procedure that simultaneously incorporates dependence within and between spatial resolutions in a recursively partitioned spatial domain. Statistical and computational properties of our distributed approach are investigated theoretically and in simulations. The proposed approach is used to extract new insights on autism spectrum disorder from the Autism Brain Imaging Data Exchange.

Keywords: Divide-and-conquer, Generalized method of moments, Nearest-neighbour Gaussian process, Functional connectivity, Optimal estimating functions.

1 Introduction

The proposed methods are motivated by the investigation of differences in brain functional organization between people with Autism Spectrum Disorder (ASD) and their typically developing peers. The Autism Brain Imaging Data Exchange (ABIDE) neuroimaging study of resting-state functional Magnetic Resonance Imaging (rfMRI) aggregated and publicly shared neuroimaging data on participants with ASD and neurotypical controls from 16 international

*Hector and Reich were supported by a grant from the National Science Foundation (DMS2152887). Hector was also supported by a Faculty Research and Professional Development Award from North Carolina State University.

imaging sites. rfMRI measures blood oxygenation in the absence of a stimulus or task and characterizes intrinsic brain activity (Fox and Raichle, 2007). Relationships between activated brain regions of interest (ROIs) during rest can be characterized by functional connectivity between ROIs using rfMRI data. Functional connectivity between two ROIs is typically estimated from the subject-specific correlation constructed from the rfMRI time series (He et al., 2009). To avoid the computational burden of storing and modeling a large connectivity matrix, the rfMRI time series is averaged across voxels in each ROI before computing the cross-ROI correlation and modeling its relationship with covariates. Other approaches for quantifying covariate effects on correlation are primarily univariate (see, e.g., Shehzad et al., 2014). These standard approaches are substantially underpowered to detect small effect sizes and obscure important variation within ROIs. While ABIDE data have led to some evidence that ASD can be broadly characterized as a brain dysconnection syndrome, findings have varied across studies (Uddin et al., 2013; Alaerts et al., 2014; Di Martino et al., 2014). Computationally and statistically efficient estimation of functional connectivity maps is essential in identifying ASD dysconnections. In this paper, we show how to estimate the effect of covariates including ASD on over 6.5 million within- and between-ROI correlations in approximately 5 hours.

The first component of our efficient approach is to leverage the spatial dependence within- and between all voxels in ROIs using Gaussian process models (Cressie, 1993; Banerjee et al., 2014; Cressie and Wikle, 2015). Denote the rfMRI outcomes $\{y_i(\mathbf{s})\}_{i=1}^N$ for N independent samples at one of S voxels $\mathbf{s} \in \mathcal{S}$. The joint distribution of $y_i(\mathcal{S})$ is assumed multivariate Gaussian and known up to a vector of parameters of interest $\boldsymbol{\theta}$. Without further modeling assumptions or dimension reduction techniques, maximum likelihood estimation has memory and computational complexity $O(NS^2)$ and $O(NS^3)$ respectively due to the S -dimensional covariance matrix. For inference on $\boldsymbol{\theta}$ when S is large, the crux of the problem is to adequately model the spatial dependence without storing or inverting a large covariance matrix.

This problem has received considerable attention (Sun et al., 2011; Bradley et al., 2016; Heaton et al., 2019; Liu et al., 2020). Solutions include, for example, the composite likelihood (CL) (Lindsay, 1988; Varin et al., 2011) the nearest-neighbour Gaussian process (Datta et al., 2016; Finley et al., 2019), spectral methods (Fuentes, 2007), tapered covariance functions (Furrer et al., 2006; Kaufman et al., 2008; Stein, 2013), low-rank approximations (Zimmerman, 1989; Cressie and Johannesson, 2008; Nychka et al., 2015), and combinations thereof (Sang and Huang, 2012). Stein (2013) details shortcomings of the aforementioned methods, which are primarily related to loss of statistical efficiency due to simplification of the covariance matrix or its inverse. Moreover, these methods remain computationally burdensome when S is very large, a problem which is further exacerbated when the covariance structure is nonstationary due to covariate effects on the spatial correlation parameters.

We propose a new distributed and integrated framework for big spatial data analysis. We consider a recursive partition of the spatial domain \mathcal{S} into M nested resolutions with disjoint sets of spatial observations at each resolution, and build local, fully specified distributed models in each set at the highest spatial resolution. The main technical difficulty arises from integrating inference from these distributed models over two levels of dependence: between sets in each resolution, and between resolutions. Simultaneously incorporating dependence between all sets and resolutions results in a high-dimensional dependence matrix that is computationally prohibitive to handle. The main contribution of this paper is a recursive

estimator that integrates inference over all sets and resolutions by alternating between levels of dependence at each integration step. We also propose a sequential integrated estimator that is asymptotically equivalent to the recursive integrated estimator but reduces the computational burden of recursively integrating over multiple resolutions. The resulting Multi-Resolution Recursive Integration (MRRI) framework is flexible, statistically efficient, and computationally scalable through its formulation in the MapReduce paradigm.

The rest of this paper is organized as follows. Section 2 establishes the formal problem setup, and describes the distributed model building step and the recursive integration scheme for the proposed MRRI framework. Section 3 evaluates the proposed frameworks with simulations. Section 4 presents the analysis of data from ABIDE. Proofs, additional results, ABIDE information and an R package are provided in the supplement.

2 Recursive Model Integration Framework

2.1 Problem set-up

Suppose we observe $y_i(\mathbf{s}) = \alpha_i(\mathbf{s}) + \epsilon_i(\mathbf{s})$ the i th observation at location $\mathbf{s} \in \mathbb{R}^d$, $i = 1, \dots, N$ independently and $\mathbf{s} \in \mathcal{S}$ a set of S locations, where $\alpha_i(\cdot)$ characterizes the spatial variations and $\epsilon_i(\cdot)$ is an independent normally distributed measurement error with mean 0 and variance σ^2 independent of $\alpha_i(\cdot)$. Further, suppose for each independent replicate i that we observe q explanatory variables $\mathbf{X}_i(\mathbf{s}) \in \mathbb{R}^q$. We denote by $\mathcal{S} = \{\mathbf{s}_j\}_{j=1}^S$ the set of locations and define $y_i(\mathcal{S}) = \{y_i(\mathbf{s}_j)\}_{j=1}^S$ and $\mathbf{X}_i(\mathcal{S}) = \{\mathbf{X}_i(\mathbf{s}_j)\}_{j=1}^S$.

In Section 4, \mathcal{S} is the set of voxels in the left and right precentral gyri, visualized in Figure 1, and $d = 3$. Outcomes $\{y_i(\mathbf{s})\}_{i=1}^N$ consist of the thinned rfMRI time series at voxel \mathbf{s} for ABIDE participants passing quality control, where the thinning removes every second time point to remove autocorrelation; autocorrelation plots are provided in the supplement. Thinning avoids the bias occasionally introduced by other approaches (Monti, 2011) and respects usual rfMRI autocorrelation assumptions (Arbabshirani et al., 2014). Specifically, for participant $n \in \{1, \dots, 774\}$ and voxel $\mathbf{s} \in \mathcal{S}$ with a (centered and standardized) time series of length $2T_n$, the outcome $y_i(\mathbf{s})$ consists of the rfMRI outcome at time point $t \in \{2, 4, \dots, 2T_n\}$, where $i = t + \sum_{n' < n} T_{n'}$ indexes the participants and time points. This thinning results in $N = 75888$ observations of $y_i(\mathbf{s})$ that are independent across $i = 1, \dots, N$. While we focus on two ROIs for simplicity of exposition, our approach generalizes to multiple ROIs. Variables $\mathbf{X}_i(\mathbf{s}) = \mathbf{X}_i$ consist of an intercept, ASD status, age, sex and the age by ASD status interaction.

We assume that $\alpha_i(\cdot)$ is a Gaussian Process with mean function $\mu\{\cdot; \mathbf{X}_i(\cdot), \boldsymbol{\beta}\}$ and positive-definite covariance function $C_\alpha\{\cdot, \cdot; \mathbf{X}_i(\cdot), \boldsymbol{\gamma}\}$. We further assume that $\mu\{\mathcal{S}; \mathbf{X}_i(\mathcal{S}), \boldsymbol{\beta}\}$ is known up to a q_1 -dimensional vector of parameters $\boldsymbol{\beta}$, and $C_\alpha\{\mathcal{S}, \mathcal{S}; \mathbf{X}_i(\mathcal{S}), \boldsymbol{\gamma}\}$ is known up to a q_2 -dimensional vector of parameters, $\boldsymbol{\gamma}$: $C_\alpha\{\mathbf{s}_1, \mathbf{s}_2; \mathbf{X}_i(\mathbf{s}_1), \mathbf{X}_i(\mathbf{s}_2), \boldsymbol{\gamma}\} = \text{Cov}\{\alpha_i(\mathbf{s}_1), \alpha_i(\mathbf{s}_2)\}$. We allow the covariance to depend on $\mathbf{X}_i(\mathcal{S})$, resulting in a nonstationary covariance structure. We define $\boldsymbol{\theta} = (\boldsymbol{\beta}, \boldsymbol{\gamma}, \sigma^2) \in \mathbb{R}^p$ the parameter of interest, $p = q_1 + q_2 + 1$. In Section 4, C_α

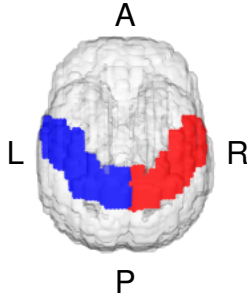


Figure 1: Left (L, blue) and right (R, red) precentral gyri. A: Anterior; P: Posterior.

borrow from Paciorek and Schervish (2003) and takes the form

$$2^{\frac{d}{2}} \tau(\mathbf{s}_j, \mathbf{s}_{j'}) \left\{ \frac{\rho_{ij'} \rho_{ij}}{(\rho_{ij'} + \rho_{ij})^2} \right\}^{\frac{d}{4}} \exp \left[\frac{-2(\mathbf{s}_{j'} - \mathbf{s}_j)^\top (\mathbf{s}_{j'} - \mathbf{s}_j)}{\rho_{ij'} + \rho_{ij}} \right], \quad (1)$$

where $\rho_{ij} = \exp\{\mathbf{X}_i^\top \boldsymbol{\rho}(\mathbf{s}_j)\}$ models the effect of \mathbf{X}_i on the correlation between voxels through $\boldsymbol{\rho}(\mathbf{s}_j) \in \mathbb{R}^q$. Both $\boldsymbol{\rho}(\mathbf{s}_j)$ and $\tau(\mathbf{s}_j, \mathbf{s}_{j'})$ are specified in Section 4.

The distribution of $y_i(\mathcal{S})$ is S -variate Gaussian with mean $\mu\{\mathcal{S}; \mathbf{X}_i(\mathcal{S}), \boldsymbol{\beta}\}$ and covariance $\mathbf{C}\{\mathcal{S}; \mathcal{S}; \mathbf{X}_i(\mathcal{S}), \boldsymbol{\gamma}, \sigma^2\} = [C_\alpha\{\mathbf{s}_r, \mathbf{s}_t; \mathbf{X}_i(\mathbf{s}_r), \mathbf{X}_i(\mathbf{s}_t), \boldsymbol{\gamma}\}]_{r,t=1}^{S,S} + \sigma^2 \mathbf{I}_S$. To overcome the difficulty of an intractable likelihood when S is large, we borrow ideas from the CL, multi-resolution approximations (MRA) and generalized method of moments (GMM).

2.2 Recursive Integration Framework

2.2.1 A Shift from Whole to Local Data Perspectives

The CL (Lindsay, 1988; Varin et al., 2011) divides \mathcal{S} into K (potentially overlapping) subsets, builds well-specified local models on the K subsets, and integrates them using working independence assumptions. The CL is attractive because it balances statistical and computational efficiencies, and the maximum CL estimator is consistent and asymptotically normal under mild regularity conditions (Cox and Reid, 2004). The main difficulty in its construction is the choice of K , which regulates both the number and the dimensionality of the marginal densities. Generally, large K is preferred as it alleviates the modeling difficulties and computational burden associated with specifying and evaluating multivariate densities. Large K , however, can result in the evaluation of a large number of low-dimensional marginals, which is computationally expensive and inefficient. When S is truly large, no choice of K is adequately statistically or computationally efficient, since the number of margins is large and their dimension remains high. To achieve a small number of low-dimensional sets, we propose a recursive partition of \mathcal{S} into multiple resolutions, with multiple sets at each resolution.

This idea is, at first blush, similar to MRA models (Nychka et al., 2015; Katzfuss, 2017; Katzfuss and Gong, 2020). Where they integrate from global to local levels, however, we build local models at the highest resolution and recursively integrate inference from the highest to the lowest resolution. Unlike MRA models, we incorporate dependence within all spatial resolutions using the GMM (Hansen, 1982) framework.

The GMM minimizes a weighted quadratic form of estimating functions and provides an intuitive mechanism for incorporating dependence between local models. Recently, [Hector and Song \(2021\)](#); [Manschot and Hector \(2022\)](#); [Hector and Reich \(2023\)](#) proposed closed-form meta-estimators for integrating estimators from dependent analyses that are asymptotically as statistically efficient as the most efficient GMM estimators but that avoid computationally expensive iterative minimization of the GMM objective function. Extending this framework to recursively partitioned spatially dependent observations, however, leads to inversion of a dependence matrix for all sets of observations that is unfortunately high-dimensional, negating the gain in computation afforded by the partition. In what follows, we propose a new weighting scheme to optimally weight GMM estimating functions and reduce their dimension for computationally tractable recursive integration of dependent models.

2.2.2 Partitioning the Spatial Domain

Let $\otimes 2$ denote the outer product of a vector with itself, namely $\mathbf{a}^{\otimes 2} = \mathbf{a}\mathbf{a}^\top$. We adopt the notation of [Katzfuss \(2017\)](#) to describe the recursive partitioning of \mathcal{S} . Denote $\mathcal{A}_0 = \mathcal{S}$ and partition \mathcal{S} into K_1 (disjoint) regions $\{\mathcal{A}_1, \dots, \mathcal{A}_{K_1}\}$ that are again partitioned into K_2 (disjoint) subregions $\{\mathcal{A}_{k_1,1}, \dots, \mathcal{A}_{k_1, K_2}\}_{k_1=1}^{K_1}$, and so on up to level M , i.e. $\mathcal{A}_{k_1 \dots k_{m-1}} = \cup_{k_m=1, \dots, K_m} \mathcal{A}_{k_1 \dots k_{m-1} k_m}$, $k_{m-1} \in \{1, \dots, K_{m-1}\}$, $m = 0, \dots, M$, where $K_0 = 1$. For completeness, let $k_0 = 0$. Figure 2 illustrates an example of a recursive partition of observations on a two-dimensional spatial domain for $M = 2$ resolutions. For resolution $m \in \{1, \dots, M\}$, denote $S_{k_1 \dots k_m}$ the size of $\mathcal{A}_{k_1 \dots k_m}$, with $S_0 = \mathcal{S}$. Further define $k_{\max} = \max k_m$ with the maximum taken over $k_m = 1, \dots, K_m$ and $m = 1, \dots, M$. Values of M and K_m should be chosen so that $S_{k_1 \dots k_M}$ and K_m , $m = 1, \dots, M$ are relatively small compared to S_0 , and we generally recommend $S_{k_1 \dots k_M} \geq 25$. The literature is replete with methods for choosing partitions; see [Heaton et al. \(2019\)](#) for an excellent review. In Section 4, we partition voxels \mathcal{S} based on nearest neighbours with $M = 3$ resolutions.

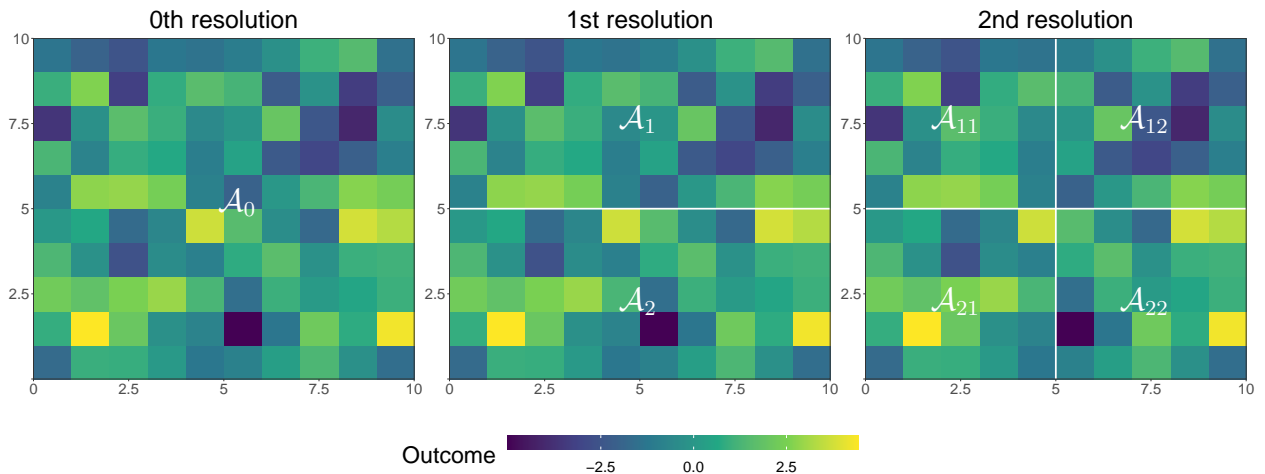


Figure 2: Example partition of observations on a two-dimensional spatial domain, $M = 2$.

2.2.3 Local Model Specification

At resolution M for $k_M \in \{1, \dots, K_M\}$, the likelihood of the data in set $\mathcal{A}_{k_1 \dots k_M}$ is given by $y_i(\mathcal{A}_{k_1 \dots k_M}) \sim \mathcal{N}[\mu\{\mathcal{A}_{k_1 \dots k_M}; \mathbf{X}_i(\mathcal{A}_{k_1 \dots k_M}), \boldsymbol{\beta}\}; \mathbf{C}\{\mathcal{A}_{k_1 \dots k_M}, \mathcal{A}_{k_1 \dots k_M}; \mathbf{X}_i(\mathcal{A}_{k_1 \dots k_M}), \boldsymbol{\gamma}, \sigma^2\}]$. We model the mean of the spatial process through $\mu\{\mathcal{A}_{k_1 \dots k_M}; \mathbf{X}_i(\mathcal{A}_{k_1 \dots k_M}), \boldsymbol{\beta}\} = \mathbf{X}_i^\top(\mathcal{A}_{k_1 \dots k_M})\boldsymbol{\beta}$. In Section 4, $\mu\{\mathbf{s}_j; \mathbf{X}_i(\mathbf{s}_j), \boldsymbol{\beta}\} = \boldsymbol{\beta}$ for $\mathbf{s}_j \in \mathcal{A}_{k_1 \dots k_M}$ due the centering of each time series, and \mathbf{C} is the nonstationary covariance function in (1) that models the effect of covariates on functional connectivity within and between the left and right precentral gyri. Due to the recursive partitioning, $S_{k_1 \dots k_M}$ is small and the full likelihood tractable. Denote the log-likelihood of the data in $\mathcal{A}_{k_1 \dots k_M}$ as $\ell_{k_1 \dots k_M}(\boldsymbol{\theta})$ and the score function as $\boldsymbol{\Psi}_{k_1 \dots k_M}(\boldsymbol{\theta}) = \nabla_{\boldsymbol{\theta}} \ell_{k_1 \dots k_M}(\boldsymbol{\theta}) = \sum_{i=1}^N \boldsymbol{\psi}_{i, k_1 \dots k_M}(\boldsymbol{\theta})$. The maximum likelihood estimator (MLE) $\hat{\boldsymbol{\theta}}_{k_1 \dots k_M}$ of $\boldsymbol{\theta}$ in $\mathcal{A}_{k_1 \dots k_M}$ is obtained by maximizing the log-likelihood, or equivalently solving $\boldsymbol{\Psi}_{k_1 \dots k_M}(\boldsymbol{\theta}) = \mathbf{0}$.

2.3 Recursive Model Integration

2.3.1 Generalized Method of Moments Approach

We now wish to recursively integrate the local models at each resolution. For $m = M, \dots, 0$, let $k_m \in \{1, \dots, K_m\}$ denote the index for the sets at resolution m . We describe a recursive GMM approach that re-estimates $\boldsymbol{\theta}$ at each resolution $M - 1$ based on an optimally weighted form of the GMM equation from the higher resolution M . At resolution $M - 1$, we define K_{M-1} estimating functions based on the score functions from resolution M :

$$\begin{aligned} \boldsymbol{\psi}_{i, k_1 \dots k_{M-1}}(\boldsymbol{\theta}) &= \{\boldsymbol{\psi}_{i, k_1 \dots k_{M-1} k_M}(\boldsymbol{\theta})\}_{k_M=1}^{K_M} \in \mathbb{R}^{pK_M}, \quad k_{M-1} = 1, \dots, K_{M-1}, \\ \boldsymbol{\Psi}_{k_1 \dots k_{M-1}}(\boldsymbol{\theta}) &= \{\boldsymbol{\Psi}_{k_1 \dots k_{M-1} k_M}(\boldsymbol{\theta})\}_{k_M=1}^{K_M} \in \mathbb{R}^{pK_M}, \quad k_{M-1} = 1, \dots, K_{M-1}. \end{aligned}$$

The estimating function $\boldsymbol{\Psi}_{k_1 \dots k_{M-1}}(\boldsymbol{\theta})$ over-identifies $\boldsymbol{\theta} \in \mathbb{R}^p$, i.e. there are several estimating functions for each parameter. Following Hansen (1982)'s GMM, we propose to minimize the quadratic form $Q_{k_1 \dots k_{M-1}}(\boldsymbol{\theta}) = \boldsymbol{\Psi}_{k_1 \dots k_{M-1}}^\top(\boldsymbol{\theta}) \mathbf{W} \boldsymbol{\Psi}_{k_1 \dots k_{M-1}}(\boldsymbol{\theta})$, with a positive semi-definite weight matrix \mathbf{W} . Hansen (1982) showed that the optimal choice of \mathbf{W} is the inverse of the covariance of $\boldsymbol{\Psi}_{k_1 \dots k_{M-1}}(\boldsymbol{\theta})$, which can be consistently estimated by $N^{-1} \mathbf{V}_{k_1 \dots k_{M-1}}(\hat{\boldsymbol{\theta}}_{k_1 \dots k_M})$,

$$\mathbf{V}_{k_1 \dots k_{M-1}}(\hat{\boldsymbol{\theta}}_{k_1 \dots k_M}) = \sum_{i=1}^N \{\boldsymbol{\psi}_{i, k_1 \dots k_{M-1}}(\hat{\boldsymbol{\theta}}_{k_1 \dots k_M})\}^{\otimes 2}$$

the variability matrix, and $\boldsymbol{\psi}_{i, k_1 \dots k_{M-1}}(\hat{\boldsymbol{\theta}}_{k_1 \dots k_M}) = \{\boldsymbol{\psi}_{i, k_1 \dots k_M}(\hat{\boldsymbol{\theta}}_{k_1 \dots k_{M-1} k_M})\}_{k_M=1}^{K_M}$. The matrix $N^{-1} \mathbf{V}_{k_1 \dots k_{M-1}}(\hat{\boldsymbol{\theta}}_{k_1 \dots k_M})$ estimates dependence between score functions from all sets in $\mathcal{A}_{k_1 \dots k_{M-1}}$ and thus captures dependence between sets $\{\mathcal{A}_{k_1 \dots k_M}\}_{k_M=1}^{K_M}$. This choice is ‘‘Hansen’’ optimal in the sense that, for all possible choices of \mathbf{W} ,

$$\hat{\boldsymbol{\theta}}_{GMM} = \arg \min_{\boldsymbol{\theta}} Q_{k_1 \dots k_{M-1}}^*(\boldsymbol{\theta}) = \arg \min_{\boldsymbol{\theta}} \boldsymbol{\Psi}_{k_1 \dots k_{M-1}}^\top(\boldsymbol{\theta}) \mathbf{V}_{k_1 \dots k_{M-1}}^{-1}(\hat{\boldsymbol{\theta}}_{k_1 \dots k_M}) \boldsymbol{\Psi}_{k_1 \dots k_{M-1}}(\boldsymbol{\theta}) \quad (2)$$

has minimum variance among estimators $\arg \min_{\boldsymbol{\theta}} Q_{k_1 \dots k_{M-1}}(\boldsymbol{\theta})$. The computation of $Q_{k_1 \dots k_{M-1}}^*(\boldsymbol{\theta})$ in (2) requires inversion of the $(pK_M) \times (pK_M)$ dimensional matrix $\mathbf{V}_{k_1 \dots k_{M-1}}^{-1}(\hat{\boldsymbol{\theta}}_{k_1 \dots k_M})$, substantially smaller than inverting the $(pS_{k_1 \dots k_{M-1}}) \times (pS_{k_1 \dots k_{M-1}})$ dimensional matrix in the

direct evaluation of the likelihood on set $\mathcal{A}_{k_1 \dots k_{M-1}}$. This yields a faster computation than a full likelihood approach on $\mathcal{A}_{k_1 \dots k_{M-1}}$. The iterative minimization in (2), however, can be time consuming because it requires computation of the score functions $\Psi_{k_1 \dots k_M}$ at each iteration.

In the spirit of [Hector and Song \(2021\)](#), a closed-form meta-estimator asymptotically equivalent to $\widehat{\theta}_{GMM}$ in (2) that is more computationally attractive is given by

$$\widehat{\theta}_{k_1 \dots k_{M-1}} = \mathbf{J}_{k_1 \dots k_{M-1}}^{-1}(\widehat{\theta}_{k_1 \dots k_M}) \mathbf{S}_{k_1 \dots k_{M-1}}(\widehat{\theta}_{k_1 \dots k_M}) \mathbf{V}_{k_1 \dots k_{M-1}}^{-1}(\widehat{\theta}_{k_1 \dots k_M}) \mathbf{T}_{k_1 \dots k_{M-1}}(\widehat{\theta}_{k_1 \dots k_M}), \quad (3)$$

where $\mathbf{S}_{k_1 \dots k_{M-1}}(\widehat{\theta}_{k_1 \dots k_M}) = -\{\nabla_{\theta} \Psi_{k_1 \dots k_{M-1}}(\theta)|_{\theta=\widehat{\theta}_{k_1 \dots k_M}}\}^{\top} \in \mathbb{R}^{p \times p K_M}$,

$$\mathbf{T}_{k_1 \dots k_{M-1}}(\widehat{\theta}_{k_1 \dots k_M}) = \left\{ \mathbf{S}_{k_1 \dots k_{M-1} k'_M}^{\top}(\widehat{\theta}_{k_1 \dots k_M}) \widehat{\theta}_{k_1 \dots k_{M-1} k'_M} \right\}_{k'_M=1}^{K_M} \in \mathbb{R}^{p K_M},$$

$$\mathbf{J}_{k_1 \dots k_{M-1}}(\widehat{\theta}_{k_1 \dots k_M}) = \mathbf{S}_{k_1 \dots k_{M-1}}(\widehat{\theta}_{k_1 \dots k_M}) \mathbf{V}_{k_1 \dots k_{M-1}}^{-1}(\widehat{\theta}_{k_1 \dots k_M}) \mathbf{S}_{k_1 \dots k_{M-1}}^{\top}(\widehat{\theta}_{k_1 \dots k_M}) \in \mathbb{R}^{p \times p}.$$

The sensitivity matrix $\mathbf{S}_{k_1 \dots k_{M-1}}(\widehat{\theta}_{k_1 \dots k_M})$ can be efficiently computed by Bartlett's identity.

When updating to the next resolution $M-2$, it is tempting to proceed again through the GMM approach and to stack estimating functions $\{\Psi_{k_1 \dots k_{M-1}}\}_{k_{M-1}=1}^{K_{M-1}}$. This would, however, result in a vector of over-identified estimating functions on θ of dimension $p K_{M-1} K_M$, and therefore inversion of a $(p K_{M-1} K_M) \times (p K_{M-1} K_M)$ dimensional covariance matrix. Recursively proceeding this way would lead to the computationally prohibitive inversion of a $(p K_1 \dots K_M) \times (p K_1 \dots K_M)$ dimensional matrix at resolution $m=0$. To avoid this difficulty, we propose weights in the spirit of optimal estimating function theory ([Heyde, 1997](#)).

2.3.2 Weighted Over-Identified Estimating Functions

We define new estimating functions at resolution $m = M-2, \dots, 0$ that optimally weight the estimating functions from resolution $m+1$,

$$\begin{aligned} \widetilde{\psi}_{i, k_1 \dots k_{M-1}}(\theta) &= -\mathbf{S}_{k_1 \dots k_{M-1}}(\widehat{\theta}_{k_1 \dots k_{M-1}}) \mathbf{V}_{k_1 \dots k_{M-1}}^{-1}(\widehat{\theta}_{k_1 \dots k_{M-1}}) \psi_{i, k_1 \dots k_{M-1}}(\theta) \in \mathbb{R}^p \\ \widetilde{\Psi}_{k_1 \dots k_{M-1}}(\theta) &= -\mathbf{S}_{k_1 \dots k_{M-1}}(\widehat{\theta}_{k_1 \dots k_{M-1}}) \mathbf{V}_{k_1 \dots k_{M-1}}^{-1}(\widehat{\theta}_{k_1 \dots k_{M-1}}) \Psi_{k_1 \dots k_{M-1}}(\theta) \in \mathbb{R}^p, \end{aligned} \quad (4)$$

where $\mathbf{S}_{k_1 \dots k_{M-1}}^{\top}(\widehat{\theta}_{k_1 \dots k_{M-1}})$ and $\mathbf{V}_{k_1 \dots k_{M-1}}(\widehat{\theta}_{k_1 \dots k_{M-1}})$ are recomputed so as to evaluate the sensitivity and variability at the estimator from resolution $M-1$. This formulation can also be viewed as the optimal projection of the estimating function $\Psi_{k_1 \dots k_{M-1}}(\theta)$ onto the parameter space of θ ([Heyde, 1997](#)). Stacking $\{\widetilde{\Psi}_{k_1 \dots k_{M-1}}(\theta)\}_{k_{M-1}=1}^{K_{M-1}}$ yields $\Psi_{k_1 \dots k_{M-2}}(\theta)$, a $p K_{M-1}$ dimensional vector of over-identifying estimating functions on θ . Defining $\mathbf{V}_{k_1 \dots k_{M-2}}(\widehat{\theta}_{k_1 \dots k_{M-1}})$ the sample covariance of $\Psi_{k_1 \dots k_{M-2}}(\theta)$ evaluated at $\widehat{\theta}_{k_1 \dots k_{M-1}}$, one can again define the closed-form meta-estimator $\widehat{\theta}_{k_1 \dots k_{M-2}}$ in the fashion of (3). This requires inversion of a $(p K_{M-1}) \times (p K_{M-1})$ -dimensional matrix, substantially smaller than inverting the $S_{k_1 \dots k_{M-2}} \times S_{k_1 \dots k_{M-2}}$ -dimensional matrix in the full likelihood on set $\mathcal{A}_{k_1 \dots k_{M-2}}$.

2.3.3 Recursive Integration Procedure

The recursive integration procedure defined by updating through Sections 2.3.1 and 2.3.2 is summarized in the supplement. At resolution $m=0$, we obtain $\psi_{i,0}(\widehat{\theta}_{k_1}) = \{\widetilde{\psi}_{i, k_1}(\widehat{\theta}_{k_1})\}_{k_1=1}^{K_1} \in$

\mathbb{R}^{pK_1} , $\Psi_0(\hat{\boldsymbol{\theta}}_{k_1}) = \{\tilde{\Psi}_{k_1}(\hat{\boldsymbol{\theta}}_{k_1})\}_{k_1=1}^{K_1} \in \mathbb{R}^{pK_1}$ and a final integrated estimator

$$\hat{\boldsymbol{\theta}}_r = \mathbf{J}_0^{-1}(\hat{\boldsymbol{\theta}}_{k_1}) \mathbf{S}_0(\hat{\boldsymbol{\theta}}_{k_1}) \mathbf{V}_0^{-1}(\hat{\boldsymbol{\theta}}_{k_1}) \left[\{\mathbf{S}_0^\top(\hat{\boldsymbol{\theta}}_{k_1})\}_j \hat{\boldsymbol{\theta}}_j \right]_{j=1}^{K_1}, \quad (5)$$

where $\mathbf{V}_0(\hat{\boldsymbol{\theta}}_{k_1}) = \sum_{i=1}^N \{\boldsymbol{\psi}_{i,0}(\hat{\boldsymbol{\theta}}_{k_1})\}^{\otimes 2}$, $\mathbf{S}_0(\hat{\boldsymbol{\theta}}_{k_1}) = -\{\nabla_{\boldsymbol{\theta}} \Psi_0(\boldsymbol{\theta})|_{\boldsymbol{\theta}=\hat{\boldsymbol{\theta}}_{k_1}}\}$ and $\mathbf{J}_0(\hat{\boldsymbol{\theta}}_{k_1}) = \mathbf{S}_0(\hat{\boldsymbol{\theta}}_{k_1}) \mathbf{V}_0^{-1}(\hat{\boldsymbol{\theta}}_{k_1}) \mathbf{S}_0^\top(\hat{\boldsymbol{\theta}}_{k_1}) \in \mathbb{R}^{p \times p}$ can be computed following the recursive procedure.

We give a toy example of the procedure. Consider a 10×10 grid of locations $\mathcal{A}_0 = \{(s_i, s_j)\}_{i,j=1}^{10}$ partitioned into $K_1 = 2$ regions $\{\mathcal{A}_1, \mathcal{A}_2\}$ that are partitioned into $K_2 = 2$ regions $\{\mathcal{A}_{11}, \mathcal{A}_{12}, \mathcal{A}_{21}, \mathcal{A}_{22}\}$, illustrated in Figure 2. We compute $\hat{\boldsymbol{\theta}}_r$ as follows:

1. For $m = 2$, compute the kernel score functions $\boldsymbol{\psi}_{i,k_1 k_2}(\boldsymbol{\theta})$, $i = 1, \dots, N$, to obtain MLEs $\hat{\boldsymbol{\theta}}_{k_1 k_2}$, $k_1 = 1, 2$, $k_2 = 1, 2$.
2. For $m = 1$, define $\boldsymbol{\psi}_{i,k_1}(\hat{\boldsymbol{\theta}}_{k_1 k_2}) = \{\boldsymbol{\psi}_{i,k_1 1}^\top(\hat{\boldsymbol{\theta}}_{k_1 1}), \boldsymbol{\psi}_{i,k_1 2}^\top(\hat{\boldsymbol{\theta}}_{k_1 2})\}^\top$, $i = 1, \dots, N$, so that we can compute $\mathbf{V}_{k_1}(\hat{\boldsymbol{\theta}}_{k_1 k_2}) = \sum_{i=1}^N \{\boldsymbol{\psi}_{i,k_1}(\hat{\boldsymbol{\theta}}_{k_1 k_2})\}^{\otimes 2}$. This allows us to estimate the sensitivity with $\mathbf{S}_{k_1}(\hat{\boldsymbol{\theta}}_{k_1 k_2})$ and obtain $\hat{\boldsymbol{\theta}}_{k_1}$ in (3) for $k_1 = 1, 2$.
3. For $m = 0$, recursively compute $\mathbf{V}_0(\hat{\boldsymbol{\theta}}_{k_1}) = \sum_{i=1}^N [\{\tilde{\boldsymbol{\psi}}_{i,k_1}(\hat{\boldsymbol{\theta}}_{k_1})\}_{k_1=1}^2]^{\otimes 2}$, $\mathbf{S}_0(\hat{\boldsymbol{\theta}}_{k_1})$, $\mathbf{J}_0(\hat{\boldsymbol{\theta}}_{k_1})$:
 - (a) Compute the kernel score functions $\boldsymbol{\psi}_{i,k_1 k_2}(\hat{\boldsymbol{\theta}}_{k_1})$, $i = 1, \dots, N$, $k_1 = 1, 2$, $k_2 = 1, 2$.
 - (b) Define $\boldsymbol{\psi}_{i,k_1}(\hat{\boldsymbol{\theta}}_{k_1}) = \{\boldsymbol{\psi}_{i,k_1 1}^\top(\hat{\boldsymbol{\theta}}_{k_1}), \boldsymbol{\psi}_{i,k_1 2}^\top(\hat{\boldsymbol{\theta}}_{k_1})\}^\top$ so that we can compute $\mathbf{V}_{k_1}(\hat{\boldsymbol{\theta}}_{k_1}) = \sum_{i=1}^N \{\boldsymbol{\psi}_{i,k_1}(\hat{\boldsymbol{\theta}}_{k_1})\}^{\otimes 2}$, allowing us to estimate the sensitivity with $\mathbf{S}_{k_1}(\hat{\boldsymbol{\theta}}_{k_1})$, $k_1 = 1, 2$.
 - (c) Compute $\tilde{\boldsymbol{\psi}}_{i,k_1}(\hat{\boldsymbol{\theta}}_{k_1}) = \mathbf{S}_{k_1}(\hat{\boldsymbol{\theta}}_{k_1}) \mathbf{V}_{k_1}^{-1}(\hat{\boldsymbol{\theta}}_{k_1}) \boldsymbol{\psi}_{i,k_1}(\hat{\boldsymbol{\theta}}_{k_1})$, $k_1 = 1, 2$.

Then compute $\mathbf{V}_0(\hat{\boldsymbol{\theta}}_{k_1})$, $\mathbf{S}_0(\hat{\boldsymbol{\theta}}_{k_1})$ and $\mathbf{J}_0(\hat{\boldsymbol{\theta}}_{k_1})$ to obtain $\hat{\boldsymbol{\theta}}_r$ in (5).

One evaluation at resolution M has computation and memory complexities of $O\{N(pS_{k_1 \dots k_M})^3\}$ and $O\{N(pS_{k_1 \dots k_M})^2\}$ respectively. This evaluation is repeated M times across the recursive integration procedure. The recursive loop inverts each $(pK_m) \times (pK_m)$ covariance matrix $O(M)$ times, adding computation and memory complexities $O\{M(pK_m)^3\}$ and $O\{M(pK_m)^2\}$ respectively. At each resolution m , inversions and the computation of the K_m estimators $\hat{\boldsymbol{\theta}}_{k_1 \dots k_m}$ can be done in parallel across K_m computing nodes to further reduce computational costs. This yields computation and memory complexities, respectively, of

$$O \left[\sum_{m=1}^M \left\{ N(pS_{k_1 \dots k_M})^3 + \max_{k_m=1, \dots, K_m} NM(pk_m)^3 \right\} \right] = O \left\{ NM(pS_{k_1 \dots k_M})^3 + NM^2(pk_{\max})^3 \right\}$$

$$O \left[\sum_{m=1}^M \left\{ N(pS_{k_1 \dots k_M})^2 + \max_{k_m=1, \dots, K_m} NM(pk_m)^2 \right\} \right] = O \left\{ NM(pS_{k_1 \dots k_M})^2 + NM^2(pk_{\max})^2 \right\}.$$

Finally, the computation of $\hat{\boldsymbol{\theta}}_{k_1 \dots k_m}$ requires no iterative minimization of an objective function, substantially reducing computational costs. The procedure can be fully run on a distributed system, meaning that at no point do the data need to be loaded on a central server or the full $S \times S$ covariance matrix stored.

2.4 Multi-Resolution Estimating Function Theory

Let Θ the parameter space of $\boldsymbol{\theta}$, and denote by $\boldsymbol{\theta}_0$ the true value of $\boldsymbol{\theta}$, defined formally by assumptions in the supplement. In this section, we study the asymptotic properties of $\widehat{\boldsymbol{\theta}}_r$ by formalizing a multi-resolution estimating function theory. To do this, define population versions of the estimating functions, their variability and their sensitivity: for $k_m = 1, \dots, K_m$, $\phi_{i,k_1 \dots k_m}(\boldsymbol{\theta}) = \boldsymbol{\psi}_{i,k_1 \dots k_m}(\boldsymbol{\theta})$ for $m = M, M-1$, and

$$\begin{aligned} \widetilde{\phi}_{i,k_1 \dots k_m}(\boldsymbol{\theta}) &= \mathbf{s}_{k_1 \dots k_m}(\boldsymbol{\theta}) \mathbf{v}_{k_1 \dots k_m}^{-1}(\boldsymbol{\theta}) \phi_{i,k_1 \dots k_m}(\boldsymbol{\theta}), \quad m = M-1, \dots, 1 \\ \phi_{i,k_1 \dots k_m}(\boldsymbol{\theta}) &= \{\widetilde{\phi}_{i,k_1 \dots k_{m+1}}(\boldsymbol{\theta})\}_{k_{m+1}=1}^{K_{m+1}}, \quad m = M-2, \dots, 1, \end{aligned}$$

where, for $m = 1, \dots, M$, $\mathbf{v}_{k_1 \dots k_m}(\boldsymbol{\theta}) = \mathbb{V}_{\boldsymbol{\theta}_0} \{\phi_{i,k_1 \dots k_m}(\boldsymbol{\theta})\}$, $\mathbf{s}_{k_1 \dots k_m}^\top(\boldsymbol{\theta}) = -\mathbb{E}_{\boldsymbol{\theta}_0} \{\nabla_{\boldsymbol{\theta}} \phi_{i,k_1 \dots k_m}(\boldsymbol{\theta})\}$ and $\mathbf{j}_{k_1 \dots k_m}(\boldsymbol{\theta}) = \mathbf{s}_{k_1 \dots k_m}(\boldsymbol{\theta}) \mathbf{v}_{k_1 \dots k_m}^{-1}(\boldsymbol{\theta}) \mathbf{s}_{k_1 \dots k_m}^\top(\boldsymbol{\theta})$ are the variability, sensitivity and Godambe information (Godambe, 1991) matrices, respectively, in $\mathcal{A}_{k_1 \dots k_m}$. Let $\phi_{i,0}(\boldsymbol{\theta}) = \{\widetilde{\phi}_{i,k_1}(\boldsymbol{\theta})\}_{k_1=1}^{K_1}$, and define $\mathbf{v}_0(\boldsymbol{\theta}) = \mathbb{V}_{\boldsymbol{\theta}_0} \{\phi_{i,0}(\boldsymbol{\theta})\}$, $\mathbf{s}_0^\top(\boldsymbol{\theta}) = -\mathbb{E}_{\boldsymbol{\theta}_0} \{\nabla_{\boldsymbol{\theta}} \phi_{i,0}(\boldsymbol{\theta})\}$ and $\mathbf{j}_0(\boldsymbol{\theta}) = \mathbf{s}_0(\boldsymbol{\theta}) \mathbf{v}_0^{-1}(\boldsymbol{\theta}) \mathbf{s}_0^\top(\boldsymbol{\theta})$. We assume throughout that $\mathbf{v}_{k_1 \dots k_m}(\boldsymbol{\theta}_0)$ and $\mathbf{v}_0(\boldsymbol{\theta}_0)$ are positive definite.

Under appropriate assumptions on the score functions $\boldsymbol{\Psi}_{k_1 \dots k_M}(\boldsymbol{\theta})$, namely unbiasedness, uniqueness of the root and additivity, the K_M estimators $\widehat{\boldsymbol{\theta}}_{k_1 \dots k_M}$ from the M th resolution are consistent for $\boldsymbol{\theta}_0$ and semi-parametrically efficient within each $\mathcal{A}_{k_1 \dots k_M}$, $k_M = 1, \dots, K_M$. Moreover, under appropriate conditions, $\widehat{\boldsymbol{\theta}}_{k_1 \dots k_{M-1}}$ is consistent and Hansen optimal by Hector and Song (2021). Finally, at each resolution, an optimal estimator is derived from the optimal GMM function (Hansen, 1982) and from optimal estimating function theory (Heyde, 1997). This results in a highly efficient integrated estimator $\widehat{\boldsymbol{\theta}}_r$ in (5) that fully uses the dependence within and between each resolution. This result is shown formally in Theorem 1.

Theorem 1. *Under assumptions given in the supplement as $N \rightarrow \infty$, $\widehat{\boldsymbol{\theta}}_r$ in (5) is consistent and $\sqrt{N}(\widehat{\boldsymbol{\theta}}_r - \boldsymbol{\theta}_0) \xrightarrow{d} \mathcal{N}\{\mathbf{0}, \mathbf{j}_0^{-1}(\boldsymbol{\theta}_0)\}$.*

The proof proceeds by induction after establishing consistency and asymptotic normality of the integrated estimators at resolution $M-1$. It uses a recursive Taylor expansion at each resolution to establish the appropriate convergence rate of the estimating function. Large sample confidence intervals for $\boldsymbol{\theta}_0$ can be constructed by combining Theorem 1 and the following Corollary, whose proof follows from the proof of Theorem 1 and is omitted.

Corollary 1. *Under assumptions given in the supplement as $N \rightarrow \infty$, $\mathbf{J}_0^{-1}(\widehat{\boldsymbol{\theta}}_r)$ is a consistent estimator of the asymptotic covariance of $\widehat{\boldsymbol{\theta}}_r$ in (5).*

2.5 Sequential Model Integration Framework

The most time consuming step in the recursive integration procedure requires a recursive update of the weights each time a new estimator of $\boldsymbol{\theta}$ is computed at resolution $m = M-2, \dots, 0$, as illustrated on the left of Figure 3. This is because the weight matrices $\mathbf{V}_{k_1 \dots k_m}(\widehat{\boldsymbol{\theta}}_{k_1 \dots k_{m+1}})$ and $\mathbf{S}_{k_1 \dots k_m}(\widehat{\boldsymbol{\theta}}_{k_1 \dots k_{m+1}})$ are evaluated at $\widehat{\boldsymbol{\theta}}_{k_1 \dots k_{m+1}}$. This recursive integration procedure has time complexity which depends on M^2 , which may be undesirably slow. We propose an alternate sequential integration scheme that evaluates the weight at the estimator

from the M th resolution, $\widehat{\boldsymbol{\theta}}_{k_1 \dots k_M}$, a consistent estimator for $\boldsymbol{\theta}$, illustrated on the right of Figure 3. The sequential integration procedure replaces the recursive evaluation of the weights with a sequential update by computing $\mathbf{V}_{k_1 \dots k_m}(\widehat{\boldsymbol{\theta}}_{k_1 \dots k_m})$ and $\mathbf{S}_{k_1 \dots k_m}(\widehat{\boldsymbol{\theta}}_{k_1 \dots k_m})$. In this fashion, no recursive update of the weights is required. We denote by $\widehat{\boldsymbol{\theta}}_s$ the sequential integrated estimator obtained by evaluating weights using $\mathbf{V}_{k_1 \dots k_m}(\widehat{\boldsymbol{\theta}}_{k_1 \dots k_m})$ and $\mathbf{S}_{k_1 \dots k_m}(\widehat{\boldsymbol{\theta}}_{k_1 \dots k_m})$. A full algorithm is provided in the supplement.

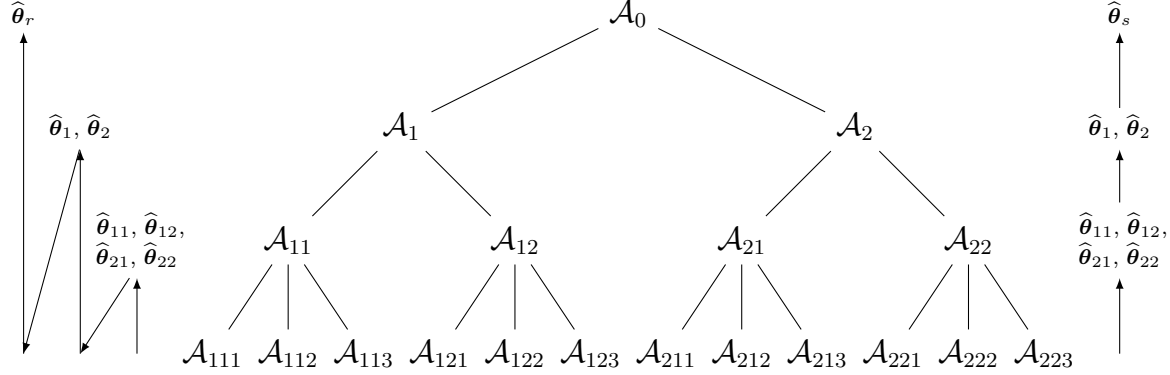


Figure 3: Example partition of \mathcal{A}_0 with $M = 3$ resolutions. Schematic propagation steps for computation of $\widehat{\boldsymbol{\theta}}_{k_1 \dots k_m}$ for recursive (left) and sequential (right) integration schemes.

Arguing as in Section 2.3.3, the computation and memory complexities of computing $\widehat{\boldsymbol{\theta}}_s$ are $O\{N(pS_{k_1 \dots k_M})^3 + NM(pk_{\max})^3\}$ and $O\{N(pS_{k_1 \dots k_M})^2 + NM(pk_{\max})^2\}$ respectively. A consequence of the proof of Theorem 1 is that $\widehat{\boldsymbol{\theta}}_s$ and $\widehat{\boldsymbol{\theta}}_r$ are asymptotically equivalent. While $\widehat{\boldsymbol{\theta}}_s$ may be computationally more advantageous, it requires that the MLEs from resolution M be close to $\boldsymbol{\theta}_0$, and may not perform as well as $\widehat{\boldsymbol{\theta}}_r$ in finite samples.

3 Simulations

We investigate the finite sample performance of the proposed recursive and sequential multi-resolution recursive integrated (MRRI) estimators $\widehat{\boldsymbol{\theta}}_r$ and $\widehat{\boldsymbol{\theta}}_s$. Throughout, \mathcal{S} consists of a square grid of evenly spaced locations. Unless otherwise specified, all simulations are on a Linux cluster using R linked to Intel’s MKL libraries with analyses at resolution M performed in parallel across $\widetilde{K} = \prod_{m=1}^M K_m$ CPUs with 1GB of RAM each. Standard errors and confidence intervals are calculated using the results in Theorem 1 and Corollary 1.

In the first set of simulations, we consider a $S = 400$ -dimensional square spatial domain $\mathcal{S} = [1, 20]^2 = \{\mathbf{s}_j\}_{j=1}^{400}$, $\mathbf{s}_j \in \mathbb{R}^2$, with $N = 10000$. The Gaussian outcomes $\{y_i(\mathcal{S})\}_{i=1}^N$ are independently simulated with means $\{\mathbf{X}_i^\top(\mathcal{S})\boldsymbol{\beta}\}_{i=1}^N$ and Gaussian spatial covariance function $C_\alpha(\mathbf{s}_j, \mathbf{s}_{j'}; \boldsymbol{\gamma}) = \tau^2 \exp\{-\rho^2(\mathbf{s}_{j'} - \mathbf{s}_j)^\top(\mathbf{s}_{j'} - \mathbf{s}_j)\}$, with $\boldsymbol{\beta}, \boldsymbol{\gamma} = (\tau^2, \rho^2)$ and nugget variance σ^2 specified below. The covariates $\mathbf{X}_i(\mathbf{s}_j) = \mathbf{X}_i$ consist of an intercept and two non-spatially varying continuous variables independently generated from a Gaussian distribution with mean 0 and variance 4. The true value of the regression coefficient is $\boldsymbol{\beta} = (0.3, 0.6, 0.8)$, the true nugget variance is $\sigma^2 = 1.6$ and the Gaussian spatial covariance function has true parameters $\tau^2 = 3$ and $\rho^2 = 0.5$. To facilitate estimation, we estimate $\boldsymbol{\theta} = \{\boldsymbol{\beta}^\top, \log(\tau^2), \log(\rho^2), \log(\sigma^2)\}$

using $\hat{\theta}_r$ and $\hat{\theta}_s$. We consider three recursive partitions of S with $M = 3$: in Setting I, $K_1 = K_2 = 2, K_3 = 4$; in Setting II, $K_1 = K_3 = 2, K_2 = 4$; in Setting III, $K_1 = 4, K_2 = K_3 = 2$. Division of the spatial domain is based on nearest neighbours as illustrated in Figure 2. We also estimate θ using two comparative approaches. Specifically, we compare to the partitioning approach (Part.) in Heaton et al. (2019) that evaluates the sum of the \tilde{K} log-likelihoods at a grid of values of τ^2, ρ^2 , estimates τ^2, ρ^2 using the values that return the highest log-likelihood, then estimates β and σ^2 using the least squares estimator and a sample variance respectively; the implementation is modified directly from the code in Heaton et al. (2019). Asymptotic standard errors are estimated as the diagonal square root of the inverse variance of the score function. We also compare to the nearest neighbour Gaussian process (NNGP) (Finley et al., 2019) using the 25 nearest neighbours; we implement this ourselves using sparse matrices in Rcpp and parallelize over \tilde{K} CPUs to make a fair comparison. Figure

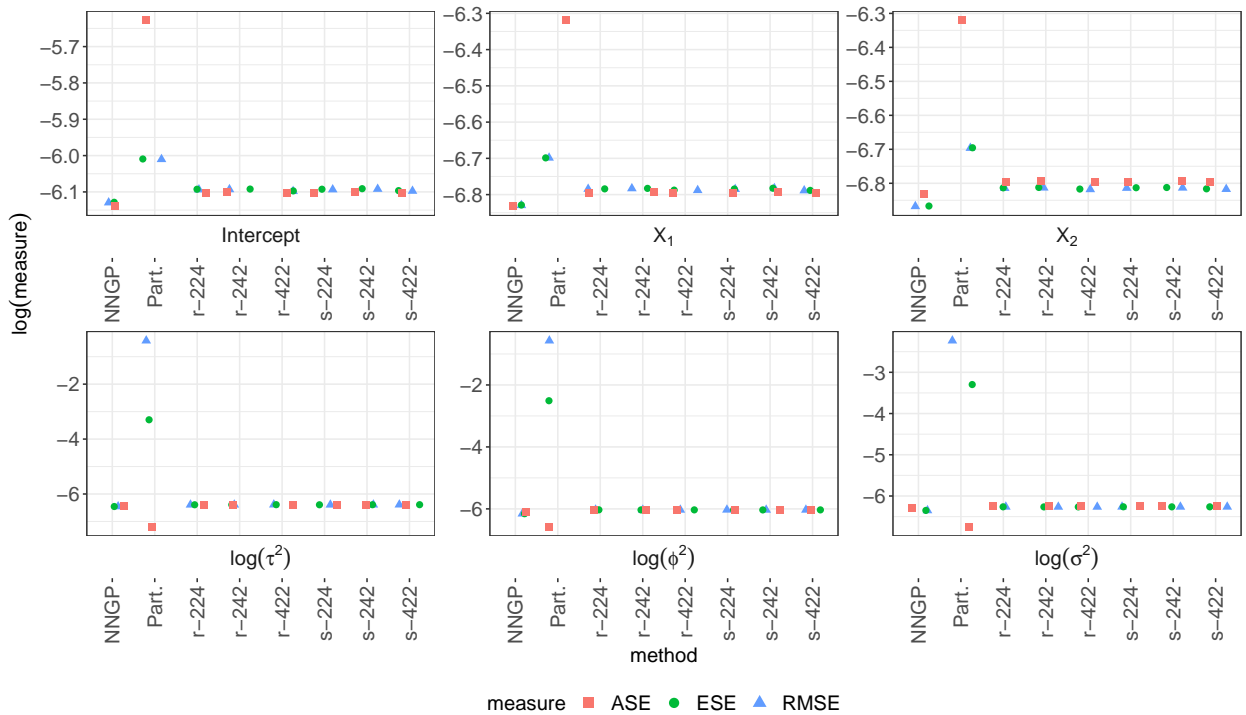


Figure 4: RMSE, ESE and ASE for estimates of each parameter using NNGP, Part., $\hat{\theta}_r$ and $\hat{\theta}_s$ in Settings I, II and III (r-224, r-242, r-422, s-224, s-242, s-422 respectively) for the first set of simulations.

4 plots the root mean squared error (RMSE), empirical standard error (ESE) and asymptotic standard error (ASE) averaged across 500 simulations for each parameter.

The near equality of RMSE and ESE in Figure 4 for our MRRI estimators $\hat{\theta}_r$ and $\hat{\theta}_s$ illustrates the near unbiasedness of our approach in large samples. Further, the near equality of ESE and ASE justifies the use of the asymptotic variance formula in Theorem 1 and Corollary 1 in large samples. Finally, negligible variation is observed across Settings I, II and III, illustrating the robustness of our approach to the chosen recursive or sequential integration scheme. The statistical inference properties of NNGP are similarly favourable,

with the NNGP appearing slightly more efficient. Finally, the partitioning approach yields estimators of β that are nearly unbiased in large samples, whereas the estimators of the covariance parameters show substantial bias. Further, standard errors of the estimators are vastly overestimated for β and underestimated for the covariance parameters, which is problematic for statistical inference. This is further illustrated in Table 1, which reports the

Table 1: 95% confidence interval coverage (CP) in percentage for first set of simulations: $S = 400$, $\theta = \{0.3, 0.6, 0.8, \log(3), \log(0.5), \log(1.6)\}$.

Method	K_1, K_2, K_3	Intercept	X_1	X_2	$\log(\sigma^2)$	$\log(\tau^2)$	$\log(\rho^2)$
$\hat{\theta}_r$	2,2,4	94	96	94	96	93	95
	2,4,2	95	96	94	96	93	95
	4,2,2	94	95	95	96	93	95
$\hat{\theta}_s$	2,2,4	94	96	94	96	93	95
	2,4,2	95	96	94	96	93	95
	4,2,2	94	95	95	96	93	95
Part.		100	100	100	0	0	0
NNGP		95	95	95	96	96	96

95% confidence interval coverage (CP) for all estimators averaged across 500 simulations. Whereas CP reaches nominal levels across parameters for MRRI and NNGP, regression and covariance parameters are respectively overcovered and undercovered using Part.

Computing times in seconds are reported in Table 2. Recursively updating weights with

Table 2: Mean elapsed time (Monte Carlo standard deviation) in seconds of $\hat{\theta}_r$, $\hat{\theta}_s$, NNGP and Part. across 500 simulation for the first set of simulations: $S = 400$, $\theta = \{0.3, 0.6, 0.8, \log(3), \log(0.5), \log(1.6)\}$.

Method	$K_1, K_2, K_3 = 2, 2, 4$	$K_1, K_2, K_3 = 2, 4, 2$	$K_1, K_2, K_3 = 4, 2, 2$	16 CPUs
$\hat{\theta}_r$	0.80 (0.092)	0.66 (0.060)	0.66 (0.060)	
$\hat{\theta}_s$	0.72 (0.084)	0.60 (0.064)	0.60 (0.064)	
NNGP				280 (140)
Part.				127 (11)

$\hat{\theta}_r$ is faster than using the weights computed at the M th layer with $\hat{\theta}_s$. In comparison, the partitioning and NNGP approaches are 212 and 467 times slower, respectively, than our estimator $\hat{\theta}_s$ with $K_1 = 4, K_2 = K_3 = 2$.

In the second set of simulations, we consider a $S = 25600$ -dimensional square spatial domain $\mathcal{S} = [1, 160]^2 = \{\mathbf{s}_j\}_{j=1}^{25600}$, $\mathbf{s}_j \in \mathbb{R}^2$, with $N = 5000$ in Setting I and $N = 2000$ in Setting II. The covariates and outcomes are generated as in the first set of simulations. The true value of θ is the same as the first set of simulations, $M = 4$, $K_1 = K_2 = K_3 = K_4 = 4$. Division of the spatial domain is based on nearest neighbours as illustrated in Figure 2. Analyses are parallelized across 16 CPUs with 2GB of RAM each. Given the performance of the partitioning approach in the first set of simulations, we only attempted to compare to the NNGP using the 100 nearest neighbours parallelized over 16 CPUs. None of the 500 simulations finished before timing out at 24 hours. Table 3 reports the RMSE, ESE, ASE, mean bias (BIAS) and CP of our MRRI estimators averaged across 500 simulations.

Table 3: Simulation metrics of $\widehat{\boldsymbol{\theta}}_r$ and $\widehat{\boldsymbol{\theta}}_s$ across 500 simulations for the second set of simulations: $S = 25600$, $\boldsymbol{\theta} = \{0.3, 0.6, 0.8, \log(3), \log(0.5), \log(1.6)\}$.

(a) Simulation metrics in Setting I.						
Estimator	Parameter	RMSE $\times 10^4$	ESE $\times 10^4$	ASE $\times 10^4$	BIAS $\times 10^5$	CP (%)
$\widehat{\boldsymbol{\theta}}_r$	Intercept	4.2	4.2	4.1	-2.7	96
	\mathbf{X}_1 effect	2.0	2.0	2.1	0.021	96
	\mathbf{X}_2 effect	2.1	2.1	2.1	0.42	94
	$\log(\tau^2)$	2.7	2.7	2.8	-1.7	96
	$\log(\rho^2)$	4.1	4.0	3.7	8.7	93
	$\log(\sigma^2)$	3.2	3.1	3.1	-3.3	96
$\widehat{\boldsymbol{\theta}}_s$	Intercept	4.2	4.2	4.1	-2.7	96
	\mathbf{X}_1 effect	2.0	2.0	2.0	0.073	96
	\mathbf{X}_2 effect	2.1	2.1	2.0	0.42	94
	$\log(\tau^2)$	2.7	2.7	2.8	-2.2	96
	$\log(\rho^2)$	4.1	4.0	3.7	9.4	93
	$\log(\sigma^2)$	3.2	3.1	3.1	-3.5	95
(b) Simulation metrics in Setting II.						
Estimator	Parameter	RMSE $\times 10^4$	ESE $\times 10^4$	ASE $\times 10^4$	BIAS $\times 10^4$	CP (%)
$\widehat{\boldsymbol{\theta}}_r$	Intercept	6.5	6.5	6.5	-0.69	95
	\mathbf{X}_1 effect	3.4	3.4	3.2	-0.073	93
	\mathbf{X}_2 effect	3.4	3.4	3.2	0.044	94
	$\log(\tau^2)$	4.5	4.5	4.4	-0.28	94
	$\log(\rho^2)$	6.4	6.3	5.9	1.3	93
	$\log(\sigma^2)$	5.1	5.1	4.8	-0.40	92
$\widehat{\boldsymbol{\theta}}_s$	Intercept	6.5	6.5	6.4	-0.72	94
	\mathbf{X}_1 effect	3.4	3.4	3.2	-0.065	93
	\mathbf{X}_2 effect	3.4	3.4	3.2	0.057	94
	$\log(\tau^2)$	4.5	4.5	4.4	-0.39	94
	$\log(\rho^2)$	6.4	6.3	5.9	1.4	93
	$\log(\sigma^2)$	5.1	5.1	4.8	-0.43	92

Again, simulation metrics in Table 3 support the use of Theorem 1 and Corollary 1 in finite samples: the RMSE, ESE and ASE are approximately equal, and the BIAS is negligible. We observe appropriate CP, with a slight undercoverage in Setting II with smaller sample size. Estimators $\widehat{\boldsymbol{\theta}}_r$ and $\widehat{\boldsymbol{\theta}}_s$ appear equivalent in these large sample size settings. The desirable statistical performance observed in the first set of simulations remains as we increase the number of resolutions, M . Finally, mean elapsed times (Monte Carlo standard deviation) in seconds are 390 (170) and 240 (110) for $\widehat{\boldsymbol{\theta}}_r$ in Settings I and II respectively, and 380 (140) and 230 (89) for $\widehat{\boldsymbol{\theta}}_s$ in Settings I and II respectively.

The third set of simulations mimics the data analysis of Section 4 with $S = 800$. We consider two ROIs, $\mathcal{S}_1 = [1, 20]^2 = \{\mathbf{s}_j\}_{j=1}^{400}$ and $\mathcal{S}_2 = [21, 40]^2 = \{\mathbf{s}_j\}_{j=401}^{800}$, $\mathbf{s}_j \in \mathbb{R}^2$. Defining $\mathcal{S} = \mathcal{S}_1 \cup \mathcal{S}_2$, the Gaussian outcomes $\{y_i(\mathcal{S})\}_{i=1}^N$, $N = 10000$, are independently simulated with mean $\{\mathbf{1}\beta\}_{i=1}^N$, $\beta = 0$, $\mathbf{1} \in \mathbb{R}^S$ a vector of one's, and the spatial covariance function in (1) with $d = 2$. The spatial variance is modeled through $\tau(\mathbf{s}_j, \mathbf{s}_{j'}) = \tau^2$, the spatial correlation is modeled through $\boldsymbol{\rho}(\mathbf{s}_j) = \boldsymbol{\rho}_1 \mathbb{1}(\mathbf{s}_j \in \mathcal{S}_1) + \boldsymbol{\rho}_2 \mathbb{1}(\mathbf{s}_j \in \mathcal{S}_2)$, and $\boldsymbol{\gamma} = \{\log(\tau^2), \boldsymbol{\rho}_1^\top, \boldsymbol{\rho}_2^\top\}^\top \in \mathbb{R}^{1+2q}$.

Here, $\mathbf{X}_i \in \mathbb{R}^q$ consists of an intercept and two non-spatially varying continuous variables independently generated from a Gaussian distribution with mean 0 and variance 1. The true values of the dependence parameters are set to $\sigma^2 = 1.6$, $\tau^2 = 3$, $\boldsymbol{\rho}_1 = (0.5, 0.5, 0.5)$ and $\boldsymbol{\rho}_2 = (0.6, 0.6, 0.6)$. We estimate $\boldsymbol{\theta} = \{\beta, \log(\tau^2), \boldsymbol{\rho}_1^\top, \boldsymbol{\rho}_2^\top, \log(\sigma^2)\}$ using $\hat{\boldsymbol{\theta}}_s$ using the recursive partition of S with $M = 3$: $K_1 = K_2 = 2$, $K_3 = 4$. Each set $\mathcal{A}_{k_1 \dots k_m}$ at resolution m is a union of the nearest neighbours in \mathcal{S}_1 and \mathcal{S}_2 separately, so that each set $\mathcal{A}_{k_1 k_2 k_3}$ consists of 25 locations from \mathcal{S}_1 and 25 locations from \mathcal{S}_2 , $\mathcal{A}_{k_1 k_2}$ consists of 100 locations from \mathcal{S}_1 and 100 locations from \mathcal{S}_2 , and so on. Analyses are parallelized across 16 CPUs with 2GB of RAM each. Table 4 reports the RMSE, ESE, ASE, BIAS and CPU of our MRRI estimator

Table 4: Simulation metrics of $\hat{\boldsymbol{\theta}}_s$ across 500 simulations for the third set of simulations: $S = 800$, $\boldsymbol{\theta} = \{0, \log(3), 0.5, 0.5, 0.5, 0.6, 0.6, 0.6, \log(1.6)\}$.

Parameter	RMSE $\times 10^3$	ESE $\times 10^3$	ASE $\times 10^3$	BIAS $\times 10^4$	CP (%)
β	1.4	1.4	1.4	-0.78	94
$\log(\tau^2)$	1.1	1.1	1.1	0.44	96
ρ_{11}	1.9	1.9	1.9	-0.57	94
ρ_{12}	1.9	1.9	1.8	-0.88	94
ρ_{13}	1.9	1.8	1.8	-1.80	93
ρ_{21}	1.9	1.9	1.9	-0.35	94
ρ_{22}	1.9	1.9	1.9	-1.20	95
ρ_{23}	1.9	1.9	1.9	-0.49	94
$\log(\sigma^2)$	1.2	1.2	1.2	-0.51	96

$\hat{\boldsymbol{\theta}}_s$ averaged across 500 simulations, where $\boldsymbol{\rho}_j = (\rho_{j1}, \rho_{j2}, \rho_{j3})$, $j = 1, 2$.

Parallelizing over $\tilde{K} = 16$ CPUs, mean elapsed time (Monte Carlo standard deviation) is 29 minutes (22 minutes). Simulation metrics in Table 4 are consistent with the results from the previous simulations: the RMSE, ESE and ASE are approximately equal, the BIAS is negligible, and the CP reaches the nominal 95% level. Further, to illustrate the high statistical power of our approach, we perform a test of the hypotheses $H_0 : \rho_{12} = \rho_{22}$ versus $H_A : \rho_{12} \neq \rho_{22}$ using the test statistic $Z = (\hat{\rho}_{12} - \hat{\rho}_{22} - \rho_0) \{ \mathbb{V}(\hat{\rho}_{12}) + \mathbb{V}(\hat{\rho}_{22}) - 2\text{Cov}(\hat{\rho}_{12}, \hat{\rho}_{22}) \}^{-1/2}$, which follows an approximate standard normal distribution under H_0 when $\rho_0 = 0$. In the context of the analysis of Section 4, this test evaluates whether ASD is associated with different spatial correlation in the left and right precentral gyri. Across the 500 simulations, the test rejects the null 100% of the time at level 0.05, illustrating the high statistical power of our approach. Using $\rho_0 = \rho_{12} - \rho_{22}$, the type-I error rate is 3.6% across the 500 simulations.

4 Estimation of Brain Functional Connectivity

We return to the motivating neuroimaging application described in Section 1. Out of 1112 ABIDE participants, 774 passed quality control: 379 with ASD, 647 males (335 with ASD) and 127 females (44 with ASD), with mean age 15 years (standard deviation 6 years). The left and right precentral gyri form the primary motor cortex and are responsible for executing voluntary movements (Bookheimer, 2013). They are two of the largest ROIs in the Harvard-Oxford atlas (FMRIB Software Library, 2018) with 1786 and 1888 voxels respectively. Many

individuals with ASD have motor deficits (Jansiewicz et al., 2006). Atypical connectivity within the left and right precentral gyri may indicate that these motor deficits are related to how these two brain regions coordinate movement. The pre-processing pipeline of rfMRI data has already been described by Craddock et al. (2013). Participant-specific data have been registered into a common template space such that voxel locations are comparable between participants in the study.

Define $\mathcal{S}_1 = \{\mathbf{s}_j\}_{j=1}^{1888}$ and $\mathcal{S}_2 = \{\mathbf{s}_j\}_{j=1889}^{3674}$ the set of voxels in the right and left precentral gyri, respectively, $d = 3$ the dimension of \mathbf{s}_j , and $\mathcal{S} = \mathcal{S}_1 \cup \mathcal{S}_2$. Voxels in the atlas outside the brain are assigned missing. Following the thinning described in Section 2.1, we obtain independent replicates $y_i(\mathbf{s}_j)$ observed at $S = 3674$ voxel locations, $i = 1, \dots, 75888$. We refer to this dataset as the “primary” dataset; as an evaluation of the robustness of our estimation approach, we compare estimates from this primary dataset to estimates from a secondary dataset, consisting of the excluded time points, with identical dimensions N and S . There is *a priori* no reason to believe the data distribution differs across primary and secondary datasets, and so comparing results across both datasets will allow us to quantify robustness of our analysis, a notoriously difficult task in analyses of rfMRI data (Uddin et al., 2017).

Let \mathbf{X}_i be corresponding observations of $q = 5$ covariates for outcome i : an intercept, ASD status (1 for ASD, 0 for neurotypical), age (centered and standardized), sex (0 for male, 1 for female) and the age (centered and standardized) by ASD status interaction. We model $\mu(\mathbf{s}_j; \mathbf{X}_i, \boldsymbol{\beta}) = \beta$, where $\mu(\mathbf{s}_j; \mathbf{X}_i, \boldsymbol{\beta})$ is the mean rfMRI time series at voxel \mathbf{s}_j . The covariance $C_\alpha(\mathbf{s}_{j'}, \mathbf{s}_j; \mathbf{X}_i, \boldsymbol{\gamma})$ is that given in equation (1) of Section 2.1 with $d = 3$ and $\tau(\mathbf{s}_j, \mathbf{s}_{j'}) = \{(\tau_1^2)^{\mathbb{1}(\mathbf{s}_j \in \mathcal{S}_1) + \mathbb{1}(\mathbf{s}_{j'} \in \mathcal{S}_1)} (\tau_2^2)^{\mathbb{1}(\mathbf{s}_j \in \mathcal{S}_2) + \mathbb{1}(\mathbf{s}_{j'} \in \mathcal{S}_2)}\}^{1/2}$. As in Section 3, the correlation is modeled through $\boldsymbol{\rho}(\mathbf{s}_j) = \boldsymbol{\rho}_1 \mathbb{1}(\mathbf{s}_j \in \mathcal{S}_1) + \boldsymbol{\rho}_2 \mathbb{1}(\mathbf{s}_j \in \mathcal{S}_2)$. Thus, $\boldsymbol{\gamma} = \{\log(\tau_1^2), \log(\tau_2^2), \boldsymbol{\rho}_1^\top, \boldsymbol{\rho}_2^\top\} \in \mathbb{R}^{2+2q}$ and $\boldsymbol{\theta} = \{\beta, \boldsymbol{\gamma}, \log(\sigma^2)\}$, with $\boldsymbol{\gamma}$ the parameter of primary interest describing the effect of covariates on functional connectivity within the left and precentral gyri. Correlation between the two ROIs is leveraged through the multivariate approach for increased precision. We interpret the effect of ASD on the correlation structure in detail in the supplement. Within each ROI, the ASD effect only influences the rate of the decay of the spatial correlation in the exponential term. An illustration of the correlation between ROIs for various values of $\rho_{j2}, \rho_{j'2}$ is provided in the supplement.

The size of each (primary and secondary) outcome dataset is 15GB. To overcome the computational burden of a whole dataset analysis, we estimate $\boldsymbol{\theta}$ using the sequential estimator $\hat{\boldsymbol{\theta}}_s$. To partition the three-dimensional spatial domain, we recursively partition \mathcal{S}_1 and \mathcal{S}_2 separately into $K_1 = 2, K_2 = K_3 = 4$ disjoint sets based on nearest neighbours, $M = 3$. The sets $\mathcal{A}_{k_1 \dots k_m}$ consist of the union of the disjoint partition sets of \mathcal{S}_1 and \mathcal{S}_2 at each resolution $m \in \{1, \dots, M\}$. A plot of the partitioning is provided in the supplement.

The analysis of the primary and secondary datasets takes 5.2 hours each when parallelized across 32 CPUs. The estimated effect and standard deviation (s.d.) of the intercept, ASD status, age, sex and age by ASD status interaction are reported in Table 5. In the primary dataset, the estimates (s.d.) of β , $\log(\sigma^2)$, $\log(\tau_1^2)$ and $\log(\tau_2^2)$ are, respectively, -0.00538 (2.03×10^{-4}), -4.05 (3.90×10^{-4}), -0.108 (2.53×10^{-4}), -0.0699 (2.48×10^{-4}). In the secondary dataset, the estimates (s.d.) of β , $\log(\sigma^2)$, $\log(\tau_1^2)$ and $\log(\tau_2^2)$ are, respectively, -0.00606 (2.03×10^{-4}), -4.05 (3.88×10^{-4}), -0.111 (2.51×10^{-4}), -0.0711 (2.46×10^{-4}). As expected, estimates of β are close to 0 and estimates of $\sigma^2 + \tau_j^2$ are close to 1 due to the centering and standardizing. We measure the agreement between standardized estimates

of $\boldsymbol{\theta}$ in the primary and secondary datasets using cosine similarity, the cosine of the angle between the two standardized vectors $\hat{\boldsymbol{\theta}}_q / \{\mathbb{V}(\hat{\boldsymbol{\theta}}_q)\}^{1/2}$, $q = 1, \dots, 14$. The cosine similarity is 0.999995, indicating a high degree of agreement between the standardized vectors.

Table 5: Estimated covariate effects and s.d. in the primary and secondary datasets.

Covariate	$\boldsymbol{\rho}_1$		$\boldsymbol{\rho}_2$	
	estimate	s.d. $\times 10^4$	estimate	s.d. $\times 10^4$
primary dataset				
Intercept	0.569	1.44	0.561	1.42
ASD status	-0.00628	1.32	-0.0046	1.27
age	-0.0221	1.07	-0.0119	0.932
sex	0.0362	1.79	0.0656	1.72
age by ASD status interaction	-0.00327	1.38	-0.00397	1.25
secondary dataset				
Intercept	0.568	1.43	0.562	1.41
ASD status	-0.0055	1.32	-0.00509	1.27
age	-0.0211	1.07	-0.0118	0.931
sex	0.0342	1.78	0.0642	1.72
age by ASD status interaction	-0.00492	1.38	-0.00586	1.25

From a practical perspective, estimates and their standard errors are virtually identical across primary and secondary datasets. Two-sample Z -tests, however, mostly reject the null that elements of $\boldsymbol{\theta}$ are equal in both datasets at the typical 0.05 level: this is a feature of the sample size and the high power of the test, rather than of true underlying differences between the two datasets, and illustrates well the challenges of robustness in analyses of rfMRI data. We calibrate the α -level of hypothesis testing procedures in our analysis by borrowing ideas from knock-offs (Barber and Candès, 2015). We estimate a data-dependent type-I error rate threshold as the 5% quantile of the observed p -values of the two-sample tests of equality between parameters in primary and secondary datasets. The Gaussian critical value corresponding to this 5% quantile is $z_{\text{crit}} = 8.60$.

Armed with this robust critical value, we evaluate whether the ASD main and interaction effects are significantly different across the two brain regions. We perform a test of the hypotheses $H_0^m : \rho_{12} = \rho_{22}$ versus $H_A^m : \rho_{12} \neq \rho_{22}$ and $H_0^i : \rho_{15} = \rho_{25}$ versus $H_A^i : \rho_{15} \neq \rho_{25}$ using the test statistic Z in Section 3, where ρ_{j2} and ρ_{j5} are the ASD main and interaction effects, respectively, in ROI \mathcal{S}_j , $j = 1, 2$. The test statistic for H_0^m versus H_A^m takes a value of 13.3 and 3.23 in the primary and secondary datasets respectively; since we reject H_0^m in the primary but not the secondary dataset, we conclude that the main ASD effect is not significantly different in the correlation structure of both brain regions. The test statistic for H_0^i versus H_A^i takes a value of 5.70 and 7.62 in the primary and secondary datasets respectively, and we conclude that the ASD by age interaction effect is not significantly different in the correlation structure of both brain regions. An analysis that excludes the age by ASD status interaction is included in the supplement and agrees with this analysis.

Summaries of distances $d_{jj'} = (\mathbf{s}_{j'} - \mathbf{s}_j)^\top (\mathbf{s}_{j'} - \mathbf{s}_j)$ are provided in the supplement. For a male participant of mean age (15.13 years), the estimated correlation structures between the right and left precentral gyri, within the right precentral gyrus, and within the left precentral gyrus, for a participant with and without ASD are, respectively, $0.915 \exp(-1.83d_{jj'})$ and

$0.915 \exp(-1.86d_{jj'})$, $0.898 \exp(-1.85d_{jj'})$ and $0.898 \exp(-1.89d_{jj'})$, and $0.933 \exp(-1.82d_{jj'})$ and $0.933 \exp(-1.84d_{jj'})$. ASD manifests as hyper-connectivity within and between the right and left precentral gyri. These findings concur with those of [Nebel et al. \(2014\)](#). These results also concur with a less powered analysis that averages each participant’s rfMRI times series at each voxel, then regresses the participants’ Pearson correlation between the right and left precentral gyri onto an intercept, ASD status, age, sex and the age by ASD status interaction. Estimates (s.d.) of covariate effects from this analysis are 0.726 (0.00759), -0.0457 (0.0101), 0.0159 (0.00745), -0.0111 (0.0137), -0.00293 (0.0101). Only the intercept, ASD status and age effects are significant at level 0.05, highlighting the superior power of our spatial approach.

5 Discussion

The proposed recursive and sequential integration estimators depend on the choice of the recursive partition of \mathcal{S} . We have suggested that this partitioning be performed such that $S_{k_1 \dots k_m}$ and K_m , $m = 1, \dots, M$ are relatively small compared to S_0 and shown through simulations that this leads to desirable statistical and computational performance. Nonetheless, the GMM is known to underestimate the variance of estimators when K_m is moderately large relative to N ; see [Hansen et al. \(1996\)](#) and others in the special issue. Thus, special care should be taken to ensure K_m is relatively low-dimensional.

In this paper, we have allowed θ to vary spatially under the constraint that it can be consistently estimated using subsets of the spatial domain \mathcal{S} . Other settings may consider a setting in which each subset is modeled through its own, subset-specific parameter. Future research should focus on the development of recursive and sequential integration rules for this setting with partially heterogeneous parameters θ following, for example, the work of [Hector and Reich \(2023\)](#) in spatially varying coefficient models. *A priori*, these extensions should follow from zero-padding the weight matrices in equations (3) and (5) and implementing an accounting system to keep track of the heterogeneous and homogeneous model parameters, although a thorough investigation needs to be performed to validate this extension.

While our approach was motivated by a comparison of functional connectivity between participants with and without ASD, the proposed methods are generally applicable to Gaussian process modeling of high-dimensional images. Our ABIDE analysis has primarily focused on the association between ASD and correlation within the left and right precentral gyri, where correlation between the two regions was modeled as a function of the within-ROI correlations. This analysis is suitable when within-ROI correlation is of primary interest. Extensions that model the between-ROI correlation through a more flexible covariance structure are of interest but beyond the scope of the present work.

Acknowledgements

The authors are grateful to the participants of the ABIDE study, and the ABIDE study organizers and members who aggregated, preprocessed and shared the ABIDE data.

A Bibliography

- Alaerts, K., Woolley, D. G., Steyaert, J., Di Martino, A., Swinnen, S. P., and Wenderoth, N. (2014). Underconnectivity of the superior temporal sulcus predicts emotion recognition deficits in autism. *Social Cognitive and Affective Neuroscience*, 9(10):1589–1600.
- Arbabshirani, M. R., Damaraju, E., Phlypo, R., Plis, S., Allen, E., Ma, S., Mathalon, D., Preda, A., Vaidya, J. G., Adali, T., and Calhoun, V. D. (2014). Impact of autocorrelation on functional connectivity. *NeuroImage*, 102(2):294–308.
- Banerjee, S., Carlin, B. P., and Gelfand, A. E. (2014). *Hierarchical modeling and analysis for spatial data*. Chapman & Hall.
- Barber, R. F. and Candès, E. J. (2015). Controlling the false discovery rate via knockoffs. *The Annals of Statistics*, 43(5):2055–2085.
- Bookheimer, S. Y. (2013). *Precentral Gyrus*, pages 2334–2335. Springer New York.
- Bradley, J. R., Cressie, N. A., and Shi, T. (2016). A comparison of spatial predictors when datasets could be very large. *Statistics Surveys*, 10:100–131.
- Cox, D. R. and Reid, N. (2004). A note on pseudolikelihood constructed from marginal densities. *Biometrika*, 91(3):729–737.
- Craddock, C., Benhajali, Y., Chu, C., Chouinard, F., Evans, A., Jakab, A., Khundrakpam, B. S., Lewis, J. D., Li, Q., Milham, M., Yan, C., and Bellec, P. (2013). The Neuro Bureau Preprocessing Initiative: open sharing of preprocessed neuroimaging data and derivatives. In *Neuroinformatics*, Stockholm, Sweden.
- Cressie, N. A. (1993). *Statistics for spatial data*. Wiley, New York.
- Cressie, N. A. and Johannesson, G. (2008). Fixed rank kriging for very large spatial data sets. *Journal of the Royal Statistical Society, Series B*, 70(1):209–226.
- Cressie, N. A. and Wikle, C. K. (2015). *Statistics for spatio-temporal data*. Wiley.
- Datta, A., Banerjee, S., Finley, A. O., and Gelfand, A. E. (2016). Hierarchical nearest-neighbour Gaussian process models for large geostatistical datasets. *Journal of the American Statistical Association*, 111(514):800–812.
- Di Martino, A., Yan, C.-G., Li, Q., Denio, E., Castellanos, F., Alaerts, K., Anderson, J., Assaf, M., Bookheimer, S., Dapretto, M., Deen, B., Delmonte, S., Dinstein, I., Ertl-Wagner, B., Fair, D., Gallagher, L., Kennedy, D., Keown, C., Keyzers, C., Lainhart, J., Lord, C., Luna, B., Menon, V., Minshew, N., Monk, C., Mueller, S., Müller, R.-A., Nebel, M., Nigg, J., O’Hearn, K., Pelphrey, K., Peltier, S., Sunaert, J. R. S., Thioux, M., Tyszka, J., Uddin, L., Wenderoth, J. V. N., Mostofsky, J. W. S., and Milham, M. (2014). The autism brain imaging data exchange: towards a large-scale evaluation of the intrinsic brain architecture in autism. *Molecular Psychiatry*, 19(6):659–667.

- Finley, A. O., Datta, A., Cook, B. D., Morton, D. C., Andersen, H. E., and Banerjee, S. (2019). Efficient algorithms for Bayesian nearest neighbour Gaussian processes. *Journal of Computational and Graphical Statistics*, 28(2):401–414.
- FMRIB Software Library (2018). FSL Atlases. <https://fsl.fmrib.ox.ac.uk/fsl/fslwiki/Atlases>. Last accessed on August 18, 2021.
- Fox, M. D. and Raichle, M. E. (2007). Spontaneous fluctuations in brain activity observed with functional magnetic resonance imaging. *Nature Reviews Neuroscience*, 8:700–711.
- Fuentes, M. (2007). Approximate likelihood for large irregularly spaced spatial data. *Journal of the American Statistical Association*, 102(477):321–331.
- Furrer, R., Genton, M. G., and Nychka, D. W. (2006). Covariance tapering for interpolation of large spatial datasets. *Journal of Computational and Graphical Statistics*, 15(3):502–523.
- Godambe, V. P. (1991). *Estimating functions*. Oxford University Press.
- Hansen, L. P. (1982). Large sample properties of generalized method of moments estimators. *Econometrica*, 50(4):1029–1054.
- Hansen, L. P., Heaton, J., and Yaron, A. (1996). Finite-sample properties of some alternative GMM estimators. *Journal of Business and Economic Statistics*, 14(3):262–280.
- He, Y., Wang, J., Wang, L., Chen, Z. J., Yan, C., Yang, H., Tang, H., Zhu, C., Gong, Q., Zang, Y., and Evans, A. C. (2009). Uncovering intrinsic modular organization of spontaneous brain activity in humans. *PLoS ONE*, 4(1):e5226.
- Heaton, M. J., Datta, A., Finley, A. O., Furrer, R., Guinness, J., Guhaniyogi, R., Gerber, F., Gramacy, R. B., Hammerling, D., Katzfuss, M., Lindgren, F., Nychka, D. W., Sun, F., and Zammit-Mangion, A. (2019). A case study competition among methods for analyzing large spatial data. *Journal of Agricultural, Biological and Environmental Statistics*, 24(398-425).
- Hector, E. C. and Reich, B. J. (2023). Distributed inference for spatial extremes modeling in high dimensions. *Journal of the American Statistical Association*, doi: 10.1080/01621459.2023.2186886.
- Hector, E. C. and Song, P. X.-K. (2021). A distributed and integrated method of moments for high-dimensional correlated data analysis. *Journal of the American Statistical Association*, 116(534):805–818.
- Heyde, C. C. (1997). *Quasi-Likelihood and its Application: a General Approach to Optimal Parameter Estimation*. Springer Series in Statistics.
- Jansiewicz, E. M., Goldber, M. C., Newschaffer, C. J., Denckla, M. B., Landa, R., and Mostofsky, S. H. (2006). Motor signs distinguish children with high functioning autism and asperger’s syndrome from controls. *Journal of autism and developmental disorders*, 36:613–621.

- Katzfuss, M. (2017). A multi-resolution approximation for massive spatial datasets. *Journal of the American Statistical Association*, 112(517):201–214.
- Katzfuss, M. and Gong, W. (2020). A class of multi-resolution approximations for large spatial datasets. *Statistica Sinica*.
- Kaufman, C. G., Schervish, M. J., and Nychka, D. W. (2008). Covariance tapering for likelihood-based estimation in large spatial data sets. *Journal of the American Statistical Association*, 103(484):1545–1555.
- Lindsay, B. G. (1988). Composite likelihood methods. *Contemporary Mathematics*, 80:220–239.
- Liu, H., Ong, Y.-S., Shen, X., and Cai, J. (2020). When Gaussian process meets big data: A review of scalable GPs. *IEEE Transactions on Neural Networks and Learning Systems*, doi: TNNLS.2019.2957109:1–19.
- Manschot, C. and Hector, E. C. (2022). Functional regression with intensively measured longitudinal outcomes: a new lens through data partitioning. *arXiv*, arXiv:2207.13014.
- Monti, M. (2011). Statistical analysis of fmri time-series: A critical review of the glm approach. *Frontiers in Human Neuroscience*, 5:28.
- Nebel, M. B., Eloyan, A., Barber, A. D., and Mostofsky, S. H. (2014). Precentral gyrus functional connectivity signatures of autism. *Frontiers in Systems Neuroscience*, 8:80.
- Nychka, D. W., Bandyopadhyay, S., Hammerling, D., Lindgren, F., and Sain, S. (2015). A multiresolution Gaussian process model for the analysis of large spatial datasets. *Journal of Computational and Graphical Statistics*, 24(2):579–599.
- Paciorek, C. and Schervish, M. (2003). Nonstationary covariance functions for gaussian process regression. *Advances in neural information processing systems*, 16.
- Sang, H. and Huang, J. Z. (2012). A full scale approximation of covariance functions for large spatial data sets. *Journal of the Royal Statistical Society, Series B*, 74(1):111–132.
- Shehzad, Z., Kelly, C., Reiss, P. T., Craddock, R. C., Emerson, J. W., McMahon, K., Copland, D. A., Castellanos, F. X., and Milham, M. P. (2014). An multivariate distance-based analytic framework for connectome-wide association studies. *Neuroimage*, 93(1):74–94.
- Stein, M. L. (2013). Statistical properties of covariance tapers. *Journal of Computational and Graphical Statistics*, 22(4):866–885.
- Sun, Y., Li, B., , and Genton, M. G. (2011). Geostatistics for large datasets. *Advances and Challenges in Space-time Modelling of Natural Events*, pages 55–77.
- Uddin, L. Q., Dajani, D. R., Voorhies, W., Bednarz, H., and Kana, R. K. (2017). Progress and roadblocks in the search for brain-based biomarkers of autism and attention-deficit/hyperactivity disorder. *Translational Psychiatry*, 7:e1218.

- Uddin, L. Q., Supekar, K., Lynch, C. J., Khouzam, A., Phillips, J., Feinstein, C., Ryali, S., and Menon, V. (2013). Salience network-based classification and prediction of symptom severity in children with autism. *Journal of the American Medical Association Psychiatry*, 70(8):869–879.
- Varin, C., Reid, N., and Firth, D. (2011). An overview of composite likelihood methods. *Statistica Sinica*, 21(1):5–42.
- Zimmerman, D. L. (1989). Computationally exploitable structure of covariance matrices and generalized covariance matrices in spatial models. *Journal of Statistical Computation and Simulation*, 32(1-2):1015.